

# Multi-port programmable silicon photonics using low-loss phase change material $\text{Sb}_2\text{Se}_3$ .

Thomas W. Radford,<sup>\*,†</sup> Idris A Ajia,<sup>†</sup> Latif Rozaqi,<sup>†</sup> Priya Deoli,<sup>†</sup> Xingzhao Yan,<sup>‡</sup> Mehdi Banakar,<sup>‡</sup> David J Thomson,<sup>‡</sup> Ioannis Zeimpekis,<sup>¶,‡</sup> Alberto Politi,<sup>†</sup> and Otto L. Muskens<sup>\*,†</sup>

<sup>†</sup>*School of Physics and Astronomy, University of Southampton, Southampton, SO17 1BJ, United Kingdom*

<sup>‡</sup>*Optoelectronics Research Centre, University of Southampton, Southampton, SO17 1BJ, United Kingdom*

<sup>¶</sup>*School of Electronics and Computer Science, University of Southampton, Southampton, SO17 1BJ, United Kingdom*

E-mail: T.Radford@soton.ac.uk; O.muskens@soton.ac.uk

## Abstract

Reconfigurable photonic devices are rapidly emerging as a cornerstone of next generation optical technologies, with wide ranging applications in quantum simulation, neuromorphic computing, and large-scale photonic processors. A central challenge in this field is identifying an optimal platform to enable compact, efficient, and scalable reconfigurability. Optical phase-change materials (PCMs) offer a compelling solution by enabling non-volatile, reversible tuning of optical properties, compatible with a wide range of device platforms and current CMOS technologies. In particular, antimony tri-selenide ( $\text{Sb}_2\text{Se}_3$ ) stands out for its ultra low-loss characteristics at telecommunication wavelengths and its reversible switching. In this work, we present an experimental platform capable of encoding multi-port operations onto the transmission matrix of a compact multimode interferometer architecture on standard 220 nm silicon photonics using *in-silico* designed digital patterns. The multi-port devices are clad with a thin film of  $\text{Sb}_2\text{Se}_3$ , which can be optically addressed using direct laser writing to provide local perturbations to the refractive index. A range of multi-port geometries from  $2 \times 2$

up to  $5 \times 5$  couplers are demonstrated, achieving simultaneous control of up to 25 matrix elements with programming accuracy of 90% relative to simulated patterns. Patterned devices remain stable with consistent optical performance across the C-band wavelengths. Our work establishes a pathway towards the development of large scale PCM-based reconfigurable multi-port devices which will allow implementing matrix operations on three orders of magnitude smaller areas than interferometer meshes.

The development of the next generation of highly reconfigurable, large-scale photonic architectures offers a critical milestone towards the realization of photonic matrix-vector multiplication accelerators,<sup>1,2</sup> convolutional operators,<sup>3</sup> optoelectronic neural networks<sup>4</sup> and microwave processors.<sup>5</sup> The interface between nanophotonics and machine learning is currently receiving tremendous interest for the promise of achieving new platforms for optical information processing.<sup>6-9</sup> Integrated photonic devices with addressable transmission matrices represent a foundational element in the advancement of analogue optical computing. Universal matrix decomposition has been well established using meshes of interferometers,<sup>10-15</sup>

yet such architectures typically occupy a large physical footprint even in modern, optimized configurations<sup>4,16</sup> which may ultimately require scale up strategies beyond a single die.<sup>17</sup>

As an alternative to cascaded single-mode devices, the potential of exploiting complex wave interference in inverse designed multimode devices has raised substantial interest.<sup>18–24</sup> Interference based components such as multimode interferometers (MMIs) may be readily employed for matrix decomposition, leveraging controlled interference to direct optical signals to individual output ports, or for mixing states across several waveguides. These devices may be optimized either during design,<sup>23</sup> creating bespoke geometries for a given application. However, in the absence of reconfigurability, practical deployment remains limited, as most implementations are inherently static. Post-fabrication control of silicon-based MMIs could be achieved through electrical heaters with limited freedom in designing the transfer function,<sup>25,26</sup> or all-optically using ultrafast induced perturbations requiring high-power laser excitation.<sup>27</sup>

Next to electrically controlled active modulation,<sup>8,14,28</sup> the development of non-volatile reconfigurable platforms can offer longer-term adaptive functionalities, reduced energy footprint and post-fabrication diversification and trimming in high-volume manufacturing.<sup>13,29–32</sup> In particular, low-loss optical phase-change materials (PCMs) offer a promising route to enable light modulation within an ultra-compact footprint.<sup>33–37</sup> Amongst the new generation of low-loss optical PCMs investigated in recent years,<sup>37</sup> antimony triselenide ( $\text{Sb}_2\text{Se}_3$ ) has become one of the main materials of choice for the development of reconfigurable silicon photonics owing to its favourable optical properties,<sup>38,39</sup> with integration of these new PCMs into CMOS foundries ongoing.<sup>40,41</sup> Reprogramming of  $\text{Sb}_2\text{Se}_3$  based PCM devices has been demonstrated via electrical<sup>34,42,43</sup> or optical actuation<sup>8,44,45</sup> and endurance of over one million write and reset cycles was shown using carefully selected parameters.<sup>46,47</sup>

In this article, we report the active reconfiguration of multimode, multi-port devices and

demonstrate the programming of permutation matrices with up to 25 elements. This new capability offers an critical step towards the development of new types of ultra-compact devices for optical information processing. Our work makes use of a standard 220 nm silicon photonics platform combined with 30 nm thin films of  $\text{Sb}_2\text{Se}_3$  to functionalize compact MMI geometries. Using direct laser writing of digital patterns, we demonstrate that combinations of weak scattering perturbations can be employed to constitute a matrix operation within the continuously coupled, multi-port device. Iteratively generated refractive perturbation patterns are used to simultaneously control up to 25 transmission matrix elements of an MMI to achieve matrix operations within a greatly reduced footprint compared to other approaches.

In this work the digital patterns are designed using an iterative optimization algorithm built around a 2.5D variational finite difference time domain (varFDTD) simulation engine. Predicting the pixel pattern required to implement a target transmission matrix is a non-trivial problem without a known analytical solution. More sophisticated alternative inverse design methodologies are available, including topology optimization,<sup>18,23,48,49</sup> non-topology black-box optimization including direct binary search and genetic algorithms,<sup>19,50–53</sup> and the application of machine learning and artificial intelligence techniques.<sup>54–56</sup> Data-driven machine-learning based optimization strategies, such as those developed in our earlier studies,<sup>54,55</sup> are effective when working with large sets of solutions. For the purpose of this study, only a small number of matrices were evaluated for a diversity of geometries, therefore a direct binary search approach was chosen to predict well-performing solutions. Our optimization process begins with the unperturbed MMI device structure, and a target transmission matrix is defined. The  $\text{Sb}_2\text{Se}_3$  region is initialized in its crystalline state (light pixels in presented figures) and divided into a predefined grid of pixels. A pixel is selected at random, and its state is switched to the amorphous phase (dark pixels in presented figures) The modified device is simulated, and a cost function used to evalu-

ate the differential in transmission between the current transmission matrix and the target. If the new configuration results in improved agreement, the change is retained and another pixel is selected, if the agreement is reduced, the pixel is reverted to its prior state. This process is repeated for  $N$  pixels, changing the state between amorphous or crystalline where appropriate in pursuit of a global minimum of the cost function.

Devices were fabricated using the 220 nm UK CORNERSTONE silicon-on-insulator (SOI) platform.<sup>57</sup> The SOI rib waveguides were etched 120 nm into the top silicon layer of the wafer. A 30 nm thick layer of  $\text{Sb}_2\text{Se}_3$  was sputter coated onto the devices before a lift-off process allowing selective deposition of PCM onto active regions of the devices. Final structures were clad with a 50 nm thin  $\text{ZnS}:\text{SiO}_2$  capping layer to prevent oxidation of the PCM and to enhance the switching performance of individual pixels. Prior to  $\text{Sb}_2\text{Se}_3$  deposition, a short argon-ion etch was employed to remove any surface oxide, as well as preserve vertical single-mode operation by embedding the PCM directly onto the waveguide structure. The multimode regions of the  $2\times 2$ ,  $3\times 3$  and  $4\times 4$  MMI devices under study have lateral dimensions of  $6\times 40\ \mu\text{m}^2$  and feature tapered waveguides at input and outputs which aid to reduce losses during out coupling. The  $5\times 5$  MMI is slightly wider to accommodate all the ports, with a dimension of  $8\times 40\ \mu\text{m}^2$ .

Switching of  $\text{Sb}_2\text{Se}_3$  was achieved through direct laser writing using a current-modulated diode laser at 639 nm wavelength (Vortran Stradus). Focused laser pulses of nanosecond time duration enable high-resolution, spatially selective programming through local amorphization of the PCM with individual pixel size of around  $0.7\ \mu\text{m}$ .<sup>44</sup> Experimentally, this was implemented by focusing the laser using a  $50\times$ , 0.42 numerical aperture (NA) long-working distance microscope objective (Mitutoyo Plan APO NIR) positioned above the sample. Reflected light was imaged onto a colour CCD camera allowing top-down imaging of the sample to position the writing spot. An electronic pulse generator (BK precision 4063b )

was used to control the pulse duration and optical power of the laser through a combination of digital and analogue voltage outputs. More information about specific switching parameters can be found in the supporting information. The objective was mounted on a three-axis stage assembly (Newport), which provided accurate positioning of the laser spot across the PCM region to program pixelated patterns of perturbations onto the device area.

The experiment requires simultaneous access to multiple device ports. However, space for in- and out-coupling using conventional multi-fibre arrays was restricted due to the working distance of the direct-write optical microscope. Therefore, a customized setup was built using a pair of free-space non-contact prisms for coupling in and out of the devices. A 3D render outlining the complete experimental process is shown in Figure 1(a) with an experimental schematic provided in Figure 1(b) and more detail outlined in the supporting information. The two right angle optical prisms were positioned above the chip at a slight tilt to allow coupling at the optimal grating angle of  $10^\circ$ . A fibre coupled step-tunable laser source (Keysight N7779C) was focused through the input prism using a  $10\times$  microscope objective and coupled into a single input waveguide of the device. On the output side, multiple grating couplers were imaged simultaneously, collecting the output signal via a separate  $5\times$  objective which projects the image of the output gratings onto an InGaAs camera (Raptor Photonics Owl-320Hs). Areas of interest corresponding to individual grating outputs were selected to quantify the relative intensity distribution across the output ports using post-processing in Python. A more detailed overview of the data collection methodology is given in the Supporting Information.

As a first demonstration of the experimental capability, we investigated the switching of a  $2\times 2$  MMI splitter. In the unperturbed state (crystalline background), the device geometry was not optimized for any particular self-imaging condition and showed significant out of plane scattering of input light and insertion loss exceeding 7.5 dB. Programming of

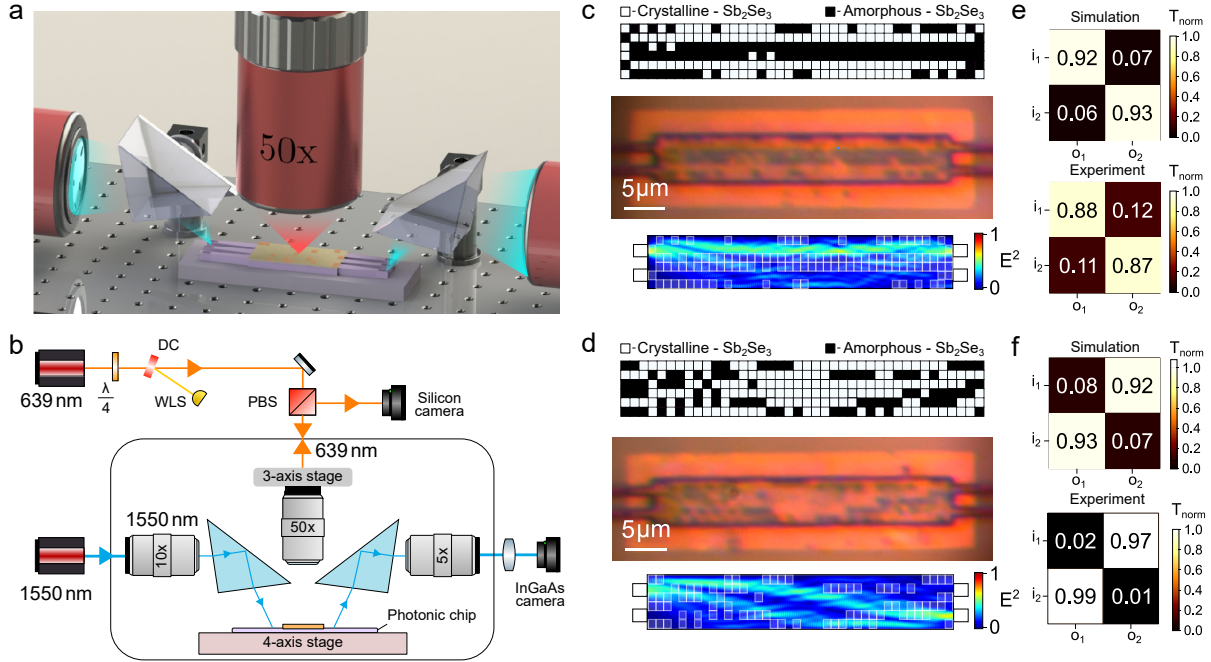


Figure 1: (a) 3D artistic render of the constructed contact free prism coupler used for direct laser writing of PCM films as well as device characterization. (b) Detailed schematic of the experimental setup. (c,d) Experimental results for the bar (c) and cross (d) states of the  $2 \times 2$  multi-port switch with designed perturbation maps (top), photograph of MMI after switching (middle), and calculated near-field map ( $|E|^2$ ) for top input (bottom). (e,f) Simulated (top) and experimental (bottom) transmission matrices for the two states.

the device resulted in the concerted action of the perturbations guiding light towards the targeted output waveguides. The chosen matrices implement an identity transformation (bar state, Figure 1c,e) and its inverse (cross state, Figure 1d,f). The simulated near field maps for the top input show that the designed pattern efficiently guides light to the corresponding output, similar simulation results are obtained for the other port (Supporting Information). In the simulation, a splitting ratio of around 92%:8% was obtained for both states, or a port extinction of 10.7 dB. Due to the spatial separation in optical path for the identity transformation, light may be routed with low crosstalk by selecting a geometry which switches straight paths of PCM to the amorphous state, effectively forming low-index channels that guide light akin to waveguides.<sup>58,59</sup>

Both experimental patterned devices exhibit strong agreement with simulated transmission behaviour, with minor deviations likely attributable to differences in perturbation strength between simulation and experiment

as well as inaccuracies in the laser writing process and alignment. The cross state outperforms the simulated pattern, achieving 15 dB port extinction. While the identity (bar) and cross configurations of the  $2 \times 2$  matrix form a relatively simple target, it serves as a clear validation of the platform's capability. In the following we place greater emphasis on the design and analysis of larger-scale devices, which offer a broader design space of non-trivial matrix operations.

Larger multi-port devices offer a broader range of potential applications, such as more powerful analogue simulation of complex systems.<sup>23</sup> However, increasing the number of ports also significantly increases the complexity of the designed pattern required to obtain a target transmission target. Figure 2 demonstrates the programming of permutation matrices using a  $3 \times 3$  MMI. The  $3 \times 3$  coupler has six available permutation matrices, which are orthogonal matrices and correspond to the symmetric group  $S_3$ . Corresponding designed pixel patterns are shown in Figure 2(a) to

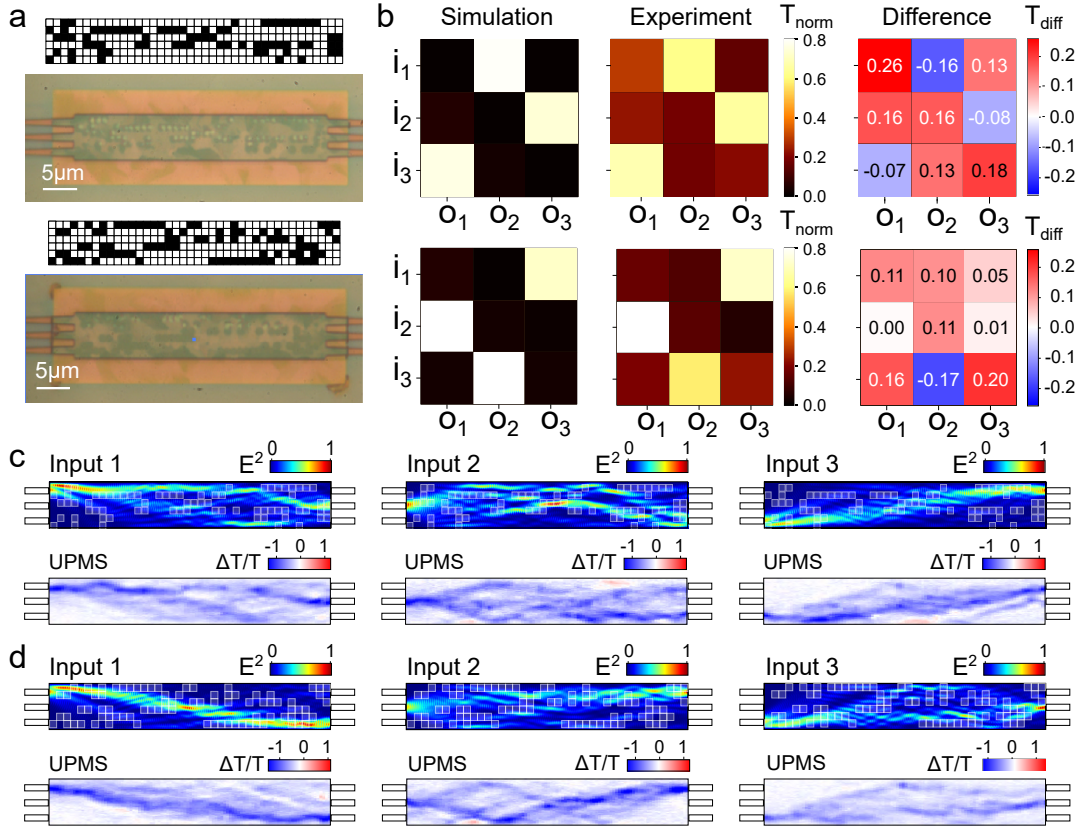


Figure 2: (a) Programmed 3×3 MMI device using patterns designed to implement two of the available permutation matrices. Recorded transmission matrices (b) show good agreement with simulated performance demonstrating average programming errors of ~12% and an average cosine similarity in excess of 0.9. UPMS measurements (c-d) are used to validate simulation models (top) by probing the electric field distribution within patterned devices.

gether with photographs of the experimentally written patterns. Due to the increased complexity of matching nine different matrix elements, it becomes more challenging to achieve the desired response with a single pixel pattern. Figure 2(b) shows resulting transmission matrices for both the simulation and the experimental realization. The simulations achieve agreement to within 92% of the ideal permutation matrix, as defined by the cosine similarity of each port, and optimized port transmissions exceeding 80% (-0.9 dB), matching previous more in-depth modelling efforts for a similar device geometry.<sup>55</sup> Experimentally, port transmissions exceeding 75% are achieved for all ports. Other non-optimized ports show a non-zero background intensity, which is attributed to imperfections in routing the signal to the output through the multiple interference of weakly scattered light paths. The difference matrix for

each case is also shown in Figure 2(b), which represents the experimental transmission minus the simulated transmission. All experimental matrix elements are normalized to a straight waveguide reference device without PCM and small changes in absolute device efficiency could cause an inaccuracy of the overall transmission as indicated by consistently positive port sums in this work.

To complement our transmission matrix measurements and gain more insight in the flow patterns generated by the perturbed MMIs, we performed Ultrafast Photomodulation Spectroscopy (UPMS) mapping. UPMS is an ultrafast pump-probe techniques developed in our previous work<sup>60,61</sup> which can be used to map the local intensity distribution in programmed devices.<sup>55,62</sup> In short, the devices were transferred to a different fibre-coupled setup and individual port combinations were measured in a

pump and probe configuration using an ultra-fast pulsed laser at 1560 nm wavelength (Menlo C-Fibre) as the probe and a frequency quadrupled 390 nm UV laser as the pump. The pump was modulated at 5 MHz using an acousto-optic modulator (AA Opto-Electronic) and focused onto the surface of the MMIs by a  $50\times$  objective with an NA of 0.55 (Mitutoyo). A Thorlabs dual-axis galvo scanner with dielectric mirrors was used to scan the pump signal across the active area of the MMI. The change in probe signal due to the perturbation induced by the pump laser was recorded using a lock-in amplifier (Zurich Instruments). Figure 2(c) and (d) show maps of the UPMS differential transmission response obtained by summing the individual signals from three output ports. These port-summed maps can be directly compared with the local intensity inside the device.<sup>60</sup> Corresponding device simulations are presented in the same figures and provide a good qualitative agreement with the observed flow patterns and routing of the signal toward the different outputs. The UPMS maps also reveal some of the parasitic paths routing light toward undesired ports. Overall the experimental maps confirm the operating principle of the programmable MMIs whereby complex flows of light are being produced by multiple weak scattering events in the digital perturbation pattern.

Provided a sufficient ability to achieve suitable design predictions, the technique should be able to program arbitrarily large devices with a comparable degree of accuracy. To test our capability, we attempted programming of  $4\times 4$  and  $5\times 5$  MMI geometries where we extend the number of degrees of freedom to up to 25 matrix elements, of which in the permutation matrices five elements are designed to non-zero and 20 are designed to be as close to zero as possible. We selected one target design for each device geometry, as presented in Figure 3(a) and (b) representing the available permutation matrices of respectively 24 (4!) and 120 (5!) for the two geometries. The experimental matrices show overall agreement with the simulation, again achieving average cosine similarities of 0.94, showing the capability of programming larger devices with up to  $5\times 5$  ports. Selected

output ports show overall high transmission exceeding 75%, and the background intensity of the other ports is reduced as the residual scattering is distributed over a larger number of ports. Insertion losses of the device (summed over all output ports) compared to a straight waveguide are modest at around 1 dB and do not depend significantly on which input, indicating that all inputs perceive nominally the same losses in the device. UPMS maps confirm the good agreement, where in particular the permutation between top and bottom ports shows accurate paths with little deviation from the design. We observe that the middle ports are more susceptible to deviations, as the interference patterns required are intricate and light get scattered more easily into neighbouring ports.

In applications of reconfigurable integrated components, it is foreseeable that devices may be required to operate across a range of input wavelengths and under varying experimental conditions. In previous studies, patterned devices with weak scattering perturbations have been demonstrated to show broadband characteristics over the telecommunications band.<sup>8,23</sup> In Figure 4 we demonstrate the spectral stability of a typical patterned device. Transmission matrices were recorded at wavelengths across the telecommunications C-band range from 1530 nm - 1570 nm. Recorded transmission values were normalized relative to a straight waveguide at the same test wavelength to compensate for the spectral response of the measurement system and grating couplers.

Figure 4 plots the cosine similarity between the simulated "ideal" device performance at 1550 nm and the recorded transmission matrix at 1 nm increments. For transmission measurements, this similarity metric is bound between 0 and 1 as negative values for transmission are non-physical in our experimental system. From this figure we observe a primarily flat response with average matrix deviations of only 11%. A randomly chosen selection of example matrices from across this range are shown in Figure 4(b) from which we demonstrate that targeted ports (i1:o4, i2:o3, i3:o3, i4:o1) remain the dominant source of transmission at all stud-

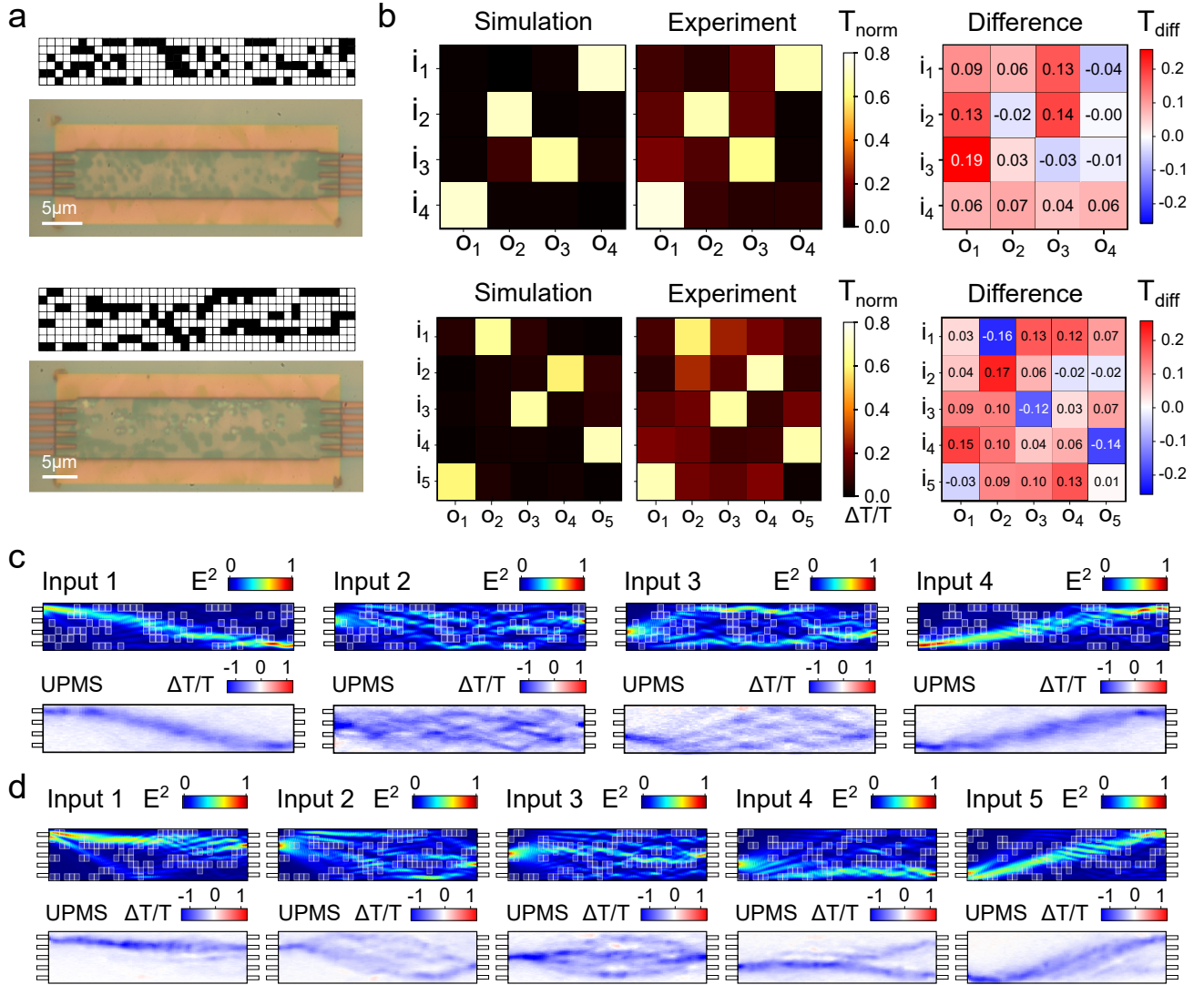


Figure 3: Programming of larger  $4 \times 4$  and  $5 \times 5$  MMI devices. Iteratively designed pixel patterns are written into a PCM film on the device, allowing implementation of an orthogonal permutation matrix. The programming error shown is the difference between simulation and recorded performance, indicating slight programming defects that occur during writing. UPMS maps further validate simulation models and indicate the distribution of electric field within the programmed device.

ied wavelengths. Figure S4 confirms this experimental trend using FDTD simulation of the patterned device, both the total and per-port values remain consistent across all test wavelengths demonstrating broadband compatibility of our devices for a range of experimental deployments.

A further important test is to ensure that a single device geometry is able to withstand multiple switching cycles. To this end Figure 4(c-d) present a  $4 \times 4$  MMI, programmed using a separate pixel pattern designed to implement an inverse identity transformation.

The device is optically programmed and subsequently de-programmed using laser pulses of differing power and duration, allowing study of the transmission characteristics throughout this process. The reported cosine similarity is again taken between simulation of the predicted pattern and the recorded values for each switching cycle. General agreement between simulation and experimental results remains good, however, through repeated switching small defects appear to develop in the capping layer of the material which results in increased insertion losses as the experiment is carried out.

These defects can be observed in the microscope images shown after thermal annealing of the sample following the 10 programming runs. Scattered light from the surface, indicates non-uniformity in the capping layer which could be caused by the mechanical expansion and stresses in the film.<sup>46</sup> While our work indicate that repeated switching is possible, further work will need to be directed toward optimization of pulse parameters and mechanical stability of the stack.

The ability to tune device characteristics enables bespoke device programmability, and also provides a promising route for post-fabrication tuning to mitigate design imperfections and increase device throughput. Nanoscale perturbation patterns can be written across a device within 2–3 minutes, a process currently limited primarily by the speed of the implementation using mechanical stages and pulse generation. Significantly faster writing will be achievable using fast laser scanning and optimized electronics and software.

Computation scalability of the approach towards larger multi-port systems depends on availability of inverse-design algorithms employed and from the accuracy with which patterns can be written into the PCM film. As the device size increases, two compounding optimization challenges emerge: the number of matrix elements requiring optimization grows quadratically with port count, and the combinatorial pixel space expands exponentially with increasing device area, presenting a clear target for future research. In our studies FDTD simulations were separately validated using experimental UPMS mapping, demonstrating good agreement with our simulation models. Other works have demonstrated scaling of computational design up to  $10 \times 10$  ports.<sup>23</sup> These available studies and our own work jointly provide evidence of the suitability of the multimode platform for a range of complex programming challenges.

Average programming errors (the difference between simulated and recorded performance) across all presented matrices remain around 10% on average, however, experimental optimization of non-targeted ports is noticeably

poorer than in simulation. This suggests that a significant source of experimental error originates from small deviations between the simulated and the programmed device. In particular, variations in spot size, shape, and pixel placement are of key importance, as even minor changes to the multimode regions of MMI geometries can dramatically alter output coupling due to the reliance on precise positioning of self-imaging points. As device dimensions grow, the importance of accurate programming further increases, as small inaccuracies compound across the larger number of programming sites required to tune the output of larger devices. Future work will therefore prioritise improvements in both the resolving power of the microscope objective and the lateral resolution of the programming stage to more faithfully reproduce simulated device geometries.

The programmed devices generally show low insertion losses compared to a straight waveguide reference and offer broadband compatibility across all C-band wavelengths with minimal deviations in the transmission matrix shape from those recorded at 1550 nm, the wavelength for which the patterns were designed. Simulations presented in supporting information show a consistent theoretical transmission of around 70% with strong optical contrast between targeted and non-targeted ports for the  $4 \times 4$  MMI under study. This spectral bandwidth enhances the applicability of the platform for systems requiring multi-wavelength operation or flexible source integration, and can likely be improved upon with the use of more advanced inverse design considering also the spectral bandwidth. Considering the typical density of traditional interferometer mesh components of around  $50 \text{ mm}^{-2}$  and the typical scaling of components with  $N(N - 1)/2$  where  $N$  is the number of input ports,<sup>1</sup> the our devices can offer an improvement of more than three orders of magnitude from several  $\text{mm}^2$  down to  $3 \times 10^{-4} \text{ mm}^2$  for a  $5 \times 5$  matrix. In conjunction with the aforementioned improvements in spatial selectivity of programming pixels, this platform therefore could enable compact and reconfigurable implementations of arbitrary unitary transformations, paving the way for pro-

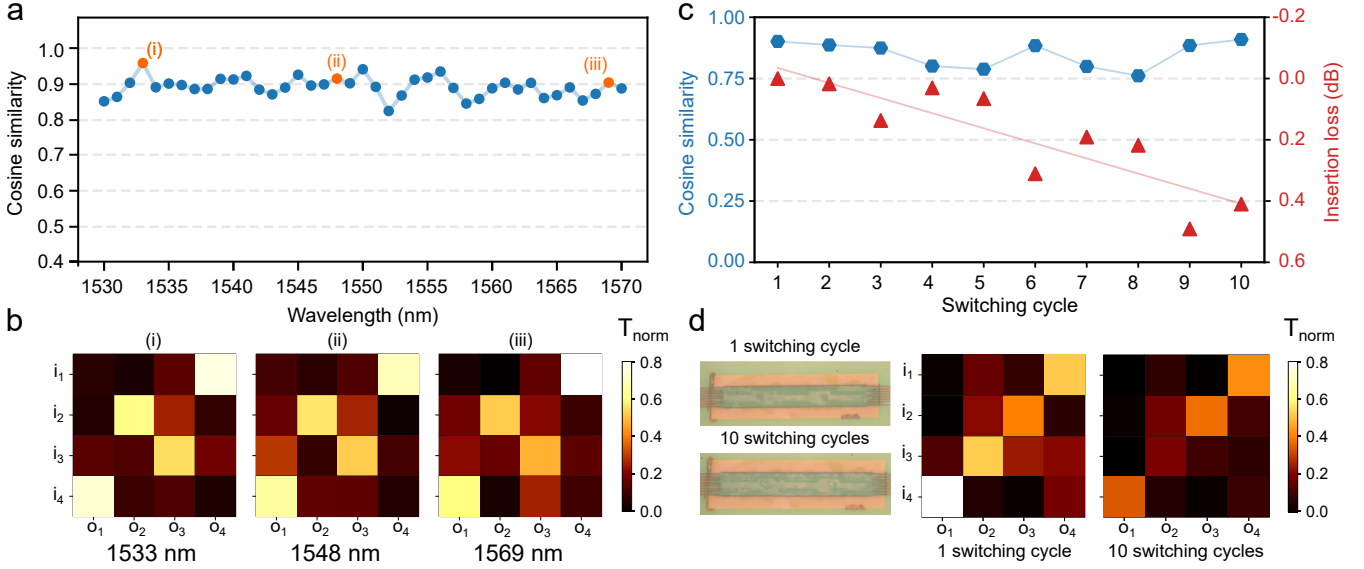


Figure 4: (a) Spectral response across C-band wavelengths of a patterned  $4 \times 4$  MMI as outlined in Figure 3. A selection of matrices are highlighted (b) from which consistent optical performance is recorded. A further pattern to implement in the inverse identity transformation is repeatedly programmed and erased using direct laser writing for both transitions (c-d) outlining the repeated reconfigurability of the presented platform, which exhibits consistent optical performance while imposing small a small insertion loss likely due to damage to the cladding material.

programmable photonic circuits in optical logic, analogue computing, and large-scale simulation systems.

$\text{Sb}_2\text{Se}_3$ -silicon integrated devices offer near-universal programmability of transmission matrices using an ultra-low-loss, passive platform. Once patterned, the device operates without the need for active control or regulation, enabling a variety of emerging optical technologies. Reconfigurable devices utilizing  $\text{Sb}_2\text{Se}_3$  are highly scalable, owing to the minimal footprint and resolution of perturbation sites, limited only by the employed fabrication process and experimental optics chosen. PCM integration enables complex matrix decomposition within a micron-scale, continuously coupled architecture, demonstrating a dramatic reduction compared to conventional approaches that rely on large interferometric meshes which and often require active stabilization. While our current work focuses on permutation operators of intensity, future studies should address the potential for programming of complex unitary operators. This will however require considerably more sophisticated methods for phase measurement at the output ports going beyond our current ca-

pabilities.

In conclusion, we have demonstrated the repeated non-volatile programming capabilities of integrated photonic devices clad with thin films of antimony tri-selenide. Using direct laser writing, we were able to experimentally map a range of target matrix operations onto a number of multi-port MMI devices, highlighting both the versatility and scalability of this approach, but also pointing out some limitations in the current implementation related to imperfections in the coupling and leakage to other ports, as well as in the repeatability studies. The patterned devices exhibit increased coupling efficiency with respect to plain MMIs of the same geometry, while maintaining modest insertion losses of, on average, 2.1 dB even for larger 5-port geometries. Resulting devices allow full control over the amplitude of all available input-output combinations, and achieve average programming accuracy of 90.7% relative to simulated device models, underscoring their suitability for a broad range of experimental systems. The proposed platform holds strong potential for applications in optical logic, photonic processors, and quantum

simulation, where compact, reconfigurable, and power-efficient components are essential.

## 1 Data availability

Supporting data used in this work is openly available from the University of Southampton repository at [doi.org/10.5258/SOTON/D3764](https://doi.org/10.5258/SOTON/D3764).

## 2 Acknowledgements

This work was supported financially by EPSRC through grants EP/M015130/1 and EP/W024683/1. Silicon photonic waveguides were manufactured through the UK Cornerstone open access Silicon Photonics rapid prototyping foundry through EPSRC grant EP/L021129/1. D.J.T. acknowledges funding from the Royal Society for his University Research Fellowship.

## References

- (1) Pérez-López, D.; Torrijos-Morán, L. Large-scale photonic processors and their applications. *npj Nanophotonics* **2025**, 2.
- (2) Zhou, H.; Dong, J.; Cheng, J.; Dong, W.; Huang, C.; Shen, Y.; Zhang, Q.; Gu, M.; Qian, C.; Chen, H.; Ruan, Z.; Zhang, X. Photonic matrix multiplication lights up photonic accelerator and beyond. *Light: Science & Applications* **2022**, 11.
- (3) Meng, X.; Zhang, G.; Shi, N.; Li, G.; Azaña, J.; Capmany, J.; Yao, J.; Shen, Y.; Li, W.; Zhu, N.; Li, M. Compact optical convolution processing unit based on multimode interference. *Nature Communications* **2023**, 14.
- (4) Xu, Z.; Zhou, T.; Ma, M.; Deng, C.; Dai, Q.; Fang, L. Large-scale photonic chiplet Taichi empowers 160-TOPS/W artificial general intelligence. *Science* **2024**, 384, 202–209.
- (5) Pérez-López, D. et al. General-purpose programmable photonic processor for advanced radiofrequency applications. *Nature Communications* **2024**, 15.
- (6) McMahon, P. L. The physics of optical computing. *Nature Reviews Physics* **2023**, 5, 717–734.
- (7) Brunner, D. et al. Roadmap on Neuromorphic Photonics. *arXiv* **2025**, 2501.07917.
- (8) Wu, C.; Jiao, Z.; Deng, H.; Huang, Y.-S.; Yu, H.; Takeuchi, I.; Ríos Ocampo, C. A.; Li, M. Reconfigurable inverse-designed phase-change photonics. *APL Photonics* **2025**, 10, 016113.
- (9) Qian, C.; Kammer, I.; Chen, H. A guidance to intelligent metamaterials and metamaterials intelligence. *Nature Communications* **2025**, 16.
- (10) Reck, M.; Zeilinger, A.; Bernstein, H. J.; Bertani, P. Experimental realization of any discrete unitary operator. *Physical review letters* **1994**, 73, 58.

- (11) Shen, Y.; Harris, N. C.; Skirlo, S.; Prabhu, M.; Baehr-Jones, T.; Hochberg, M.; Sun, X.; Zhao, S.; Larochelle, H.; Englund, D.; Soljačić, M. Deep learning with coherent nanophotonic circuits. Nature Photonics **2017**, *11*, 441–446.
- (12) Pérez, D.; Gasulla, I.; Mahapatra, P. D.; Capmany, J. Principles, fundamentals, and applications of programmable integrated photonics. Adv. Opt. Photon. **2020**, *12*, 709–786.
- (13) Bogaerts, W.; Pérez, D.; Capmany, J.; Miller, D. A. B.; Poon, J.; Englund, D.; Morichetti, F.; Melloni, A. Programmable photonic circuits. Nature **2020**, *586*, 207–216.
- (14) Chen, X.; Lin, J.; Wang, K. A Review of Silicon-Based Integrated Optical Switches. Laser & Photonics Reviews **2023**, *17*, 2200571.
- (15) Bao, J. et al. Very-large-scale integrated quantum graph photonics. Nature Photonics **2023**, *17*, 573–581.
- (16) Xie, Y.; Ke, X.; Hong, S.; Sun, Y.; Song, L.; Li, H.; Wang, P.; Dai, D. Complex-valued matrix-vector multiplication using a scalable coherent photonic processor. Science Advances **2025**, *11*, eads7475.
- (17) Seok, T. J.; Kwon, K.; Henriksson, J.; Luo, J.; Wu, M. C. Wafer-scale silicon photonic switches beyond die size limit. Optica **2019**, *6*, 490–494.
- (18) Piggott, A. Y.; Lu, J.; Lagoudakis, K. G.; Petykiewicz, J.; Babinec, T. M.; Vučković, J. Inverse design and demonstration of a compact and broadband on-chip wavelength demultiplexer. Nature Photonics **2015**, *9*, 374–377.
- (19) Shen, B.; Wang, P.; Polson, R.; Menon, R. An integrated-nanophotonics polarization beamsplitter with  $2.4 \times 2.4 \mu\text{m}^2$  footprint. Nature Photonics **2015**, *9*, 378–382.
- (20) Hughes, T. W.; Williamson, I. A. D.; Minkov, M.; Fan, S. Wave physics as an analog recurrent neural network. Science Advances **2019**, *5*.
- (21) Mohammadi Estakhri, N.; Edwards, B.; Engheta, N. Inverse-designed metastructures that solve equations. Science **2019**, *363*, 1333–1338.
- (22) Meng, Y. et al. Optical meta-waveguides for integrated photonics and beyond. Light: Science & Applications **2021**, *10*.
- (23) Nikkhah, V.; Pirmoradi, A.; Ashtiani, F.; Edwards, B.; Aflatouni, F.; Engheta, N. Inverse-designed low-index-contrast structures on a silicon photonics platform for vector–matrix multiplication. Nature Photonics **2024**, *18*, 501–508.
- (24) Fu, T.; Zang, Y.; Huang, Y.; Du, Z.; Huang, H.; Hu, C.; Chen, M.; Yang, S.; Chen, H. Photonic machine learning with on-chip diffractive optics. Nature Communications **2023**, *14*.
- (25) Álvaro Rosa; Gutiérrez, A.; Brimont, A.; Griol, A.; Sanchis, P. High performance silicon 2x2 optical switch based on a thermo-optically tunable multimode interference coupler and efficient electrodes. Opt. Express **2016**, *24*, 191–198.
- (26) Kim, S.-H.; You, J.-B.; Rhee, H.-W.; Yoo, D. E.; Lee, D.-W.; Yu, K.; Park, H.-H. High-Performance Silicon MMI Switch Based on Thermo-Optic Control of Interference Modes. IEEE Photonics Technology Letters **2018**, *30*, 1427–1430.
- (27) Bruck, R.; Vynck, K.; Lalanne, P.; Mills, B.; Thomson, D. J.; Mashanovich, G. Z.; Reed, G. T.; Muskens, O. L. All-optical spatial light modulator for reconfigurable silicon photonic circuits. Optica **2016**, *3*, 396–402.
- (28) Shekhar, S.; Bogaerts, W.; Chrostowski, L.; Bowers, J. E.; Hochberg, M.;

- Soref, R.; Shastri, B. J. Roadmapping the next generation of silicon photonics. Nature Communications **2024**, 15.
- (29) Shastri, B. J.; Tait, A. N.; Ferreira de Lima, T.; Pernice, W. H. P.; Bhaskaran, H.; Wright, C. D.; Prucnal, P. R. Photonics for artificial intelligence and neuromorphic computing. Nature Photonics **2021**, 15, 102–114.
- (30) Chen, R.; Fang, Z.; Miller, F.; Rarick, H.; Fröch, J. E.; Majumdar, A. Opportunities and Challenges for Large-Scale Phase-Change Material Integrated Electro-Photonics. ACS Photonics **2022**, 9, 3181–3195.
- (31) Fang, Z.; Chen, R.; Tossoun, B.; Cheung, S.; Liang, D.; Majumdar, A. Non-volatile materials for programmable photonics. APL Materials **2023**, 11, 100603.
- (32) Bogaerts, W.; Rahim, A. Programmable Photonics: An Opportunity for an Accessible Large-Volume PIC Ecosystem. IEEE Journal of Selected Topics in Quantum Electronics **2020**, 26, 1–17.
- (33) Fang, Z.; Chen, R.; Zheng, J.; Majumdar, A. Non-volatile reconfigurable silicon photonics based on phase-change materials. IEEE Journal of Selected Topics in Quantum Electronics **2021**, 28, 1–17.
- (34) Ríos, C.; Du, Q.; Zhang, Y.; Popescu, C.-C.; Shalaginov, M. Y.; Miller, P.; Roberts, C.; Kang, M.; Richardson, K. A.; Gu, T.; Vitale, S. A.; Hu, J. Ultra-compact nonvolatile photonics based on electrically reprogrammable transparent phase change materials. PhotonIX **2021**,
- (35) Prabhathan, P. et al. Roadmap for phase change materials in photonics and beyond. iScience **2023**, 26, 107946.
- (36) Tripathi, D.; Vyas, H. S.; Kumar, S.; Panda, S. S.; Hegde, R. Recent developments in Chalcogenide phase change material-based nanophotonics. Nanotechnology **2023**, 34, 502001.
- (37) Huang, Y.-S.; Lee, C.-Y.; Takeuchi, I.; Ríos Ocampo, C. A. Optical Phase Change Materials. Annual Review of Materials Research **2025**, 55, 255–283.
- (38) Delaney, M.; Zeimpekis, I.; Lawson, D.; Hewak, D. W.; Muskens, O. L. A new family of ultralow loss reversible phase-change materials for photonic integrated circuits: Sb<sub>2</sub>S<sub>3</sub> and Sb<sub>2</sub>Se<sub>3</sub>. Advanced Functional Materials **2020**, 30, 2002447.
- (39) Chen, X.; Lin, J.; Wang, K. A Review of Integrated Photonic Devices Using Sb<sub>2</sub>Se<sub>3</sub>. Advanced Physics Research **2025**, 4, 2400080.
- (40) Wei, M. et al. Monolithic back-end-of-line integration of phase change materials into foundry-manufactured silicon photonics. Nature Communications **2024**, 15.
- (41) Popescu, C.-C.; Kim, H. J.; Dao, K.; Mills, B.; Ranno, L.; Gu, T.; Maksimov, O.; Bhandari, H.; Hu, J. Heterogeneous integration of nonvolatile phase-change photonics. **2025**, 13375, 133750D.
- (42) Fang, Z.; Chen, R.; Zheng, J.; Khan, A. I.; Neilson, K. M.; Geiger, S. J.; Callahan, D. M.; Moebius, M. G.; Saxena, A.; Chen, M. E.; Rios, C.; Hu, J.; Pop, E.; Majumdar, A. Ultra-low-energy programmable non-volatile silicon photonics based on phase-change materials with graphene heaters. Nature Nanotechnology **2022**, 17, 842–848.
- (43) Yang, X.; Lu, L.; Li, Y.; Wu, Y.; Li, Z.; Chen, J.; Zhou, L. Non-Volatile Optical Switch Element Enabled by Low-Loss Phase Change Material. Advanced Functional Materials **2023**, 33, 2304601.
- (44) Delaney, M.; Zeimpekis, I.; Du, H.; Yan, X.; Banakar, M.; Thomson, D. J.; Hewak, D. W.; Muskens, O. L. Nonvolatile programmable silicon photonics using an ultralow-loss Sb<sub>2</sub>Se<sub>3</sub> phase change material. Science Advances **2021**, 7, eabg3500.

- (45) Wu, C.; Deng, H.; Huang, Y.-S.; Yu, H.; Takeuchi, I.; Ocampo, C. A. R.; Li, M. Freeform direct-write and rewritable photonic integrated circuits in phase-change thin films. Science Advances **2024**, 10, eadk1361.
- (46) Lawson, D.; Blundell, S.; Ebert, M.; Muskens, O. L.; Zeimpekis, I. Optical switching beyond a million cycles of low-loss phase change material Sb<sub>2</sub>Se<sub>3</sub>. Optical Materials Express **2024**, 14, 22–38.
- (47) Alam, M. S.; Laing, R.; Bolatbek, Z.; Heenkenda, R.; Gnawali, R.; Payne, T. E.; Sarangan, A.; Hendrickson, J. R.; Agha, I. Fast Cycling Speed with Multimillion Cycling Endurance of Ultra-Low Loss Phase Change Material (Sb<sub>2</sub>Se<sub>3</sub>) by Engineered Laser Pulse Irradiation. Advanced Functional Materials **2024**, 34, 2310306.
- (48) Bendsøe, M. P. Optimal shape design as a material distribution problem. Structural optimization **1989**, 1, 193–202.
- (49) Lu, L.; Joannopoulos, J. D.; Soljačić, M. Topological photonics. Nature photonics **2014**, 8, 821–829.
- (50) Digani, J.; Hon, P. W.; Davoyan, A. R. Framework for Expediting Discovery of Optimal Solutions with Blackbox Algorithms in Non-Topology Photonic Inverse Design. ACS Photonics **2022**, 9, 432–442.
- (51) Mao, S.; Cheng, L.; Zhao, C.; Khan, F. N.; Li, Q.; Fu, H. Y. Inverse Design for Silicon Photonics: From Iterative Optimization Algorithms to Deep Neural Networks. Applied Sciences **2021**, 11, 3822.
- (52) Yu, Z.; Cui, H.; Sun, X. Genetic-algorithm-optimized wideband on-chip polarization rotator with an ultrasmall footprint. Opt. Lett. **2017**, 42, 3093–3096.
- (53) Jia, W.; Menon, R.; Sensale-Rodriguez, B. Unique prospects of phase change material Sb<sub>2</sub>Se<sub>3</sub> for ultra-compact reconfigurable nanophotonic devices. Opt. Mater. Express **2021**, 11, 3007–3014.
- (54) Radford, T. W.; Wiecha, P. R.; Politi, A.; Zeimpekis, I.; Muskens, O. L. Inverse design of unitary transmission matrices in silicon photonic coupled waveguide arrays using a neural adjoint model. ACS photonics **2025**, 12, 1480–1493.
- (55) Dinsdale, N. J.; Wiecha, P. R.; Delaney, M.; Reynolds, J.; Ebert, M.; Zeimpekis, I.; Thomson, D. J.; Reed, G. T.; Lalanne, P.; Vynck, K.; others Deep learning enabled design of complex transmission matrices for universal optical components. ACS photonics **2021**, 8, 283–295.
- (56) Banerji, S.; Majumder, A.; Hamrick, A.; Menon, R.; Sensale-Rodriguez, B. Ultra-compact integrated photonic devices enabled by machine learning and digital metamaterials. OSA Continuum **2021**, 4, 602–607.
- (57) Littlejohns, C. G. et al. CORNERSTONE’s Silicon Photonics Rapid Prototyping Platforms: Current Status and Future Outlook. Applied Sciences **2020**, 10.
- (58) Shixin, G.; Haonan, R.; Jingzhe, P.; Yang, R.; Zhenqing, Z.; Shuang, Z.; Tun, C. Reconfigurable free form silicon photonics by phase change waveguides. Advanced Optical Materials **2025**, 13, 2402997.
- (59) Shang, K.; Niu, L.; Jin, H.; Wang, H.; Zhang, W.; Gan, F.; Xu, P. Non-volatile 2×2 optical switch using multimode interference in an Sb<sub>2</sub>Se<sub>3</sub>-loaded waveguide. Opt. Lett. **2024**, 49, 722–725.
- (60) Vynck, K.; Dinsdale, N. J.; Chen, B.; Bruck, R.; Khokhar, A. Z.; Reynolds, S. A.; Crudgington, L.; Thomson, D. J.; Reed, G. T.; Lalanne, P.; Muskens, O. L. Ultrafast perturbation maps as a quantitative tool for testing of multi-port photonic devices. Nature Communications **2018**, 9, 1–10.

- (61) Bruck, R.; Mills, B.; Troia, B.; Thomson, D. J.; Gardes, F. Y.; Hu, Y.; Mashanovich, G. Z.; Passaro, V.; Reed, G. T.; Muskens, O. L. Device-level characterization of the flow of light in integrated photonic circuits using ultrafast photomodulation spectroscopy. Nature Photonics **2015**, 9, 54–60.
- (62) Blundell, S.; Radford, T. W.; Ajia, I. A.; Lawson, D.; Yan, X.; Banakar, M.; Thomson, D. J.; Zeimpekis, I.; Muskens, O. L. Ultracompact programmable silicon photonics using layers of low-loss phase-change material Sb<sub>2</sub>Se<sub>3</sub> of increasing thickness. ACS photonics **2025**, 12, 1382–1391.